Selenium-Enhanced Electron Microscopic Imaging of Different Aggregate Forms of a Segment of the Amyloid β Peptide in Cells

Eva K. McGuire,[†] Michael Motskin,[‡] Benedetta Bolognesi,[§] Shane D. Bergin,[⊥] Tuomas P. J. Knowles,[§] Jeremy Skepper,[‡] Leila M. Luheshi,[§,*] David W. McComb,[†,∥] Christopher M. Dobson,[§,*] and Alexandra E. Porter[†,*]

[†]Department of Materials, Imperial College, Exhibition Road, London SW7 2AZ, United Kingdom, [‡]Department of Physiology, Development and Neuroscience, University of Cambridge, Downing Street, Cambridge CB2 3DY, United Kingdom, [§]Department of Chemistry, University of Cambridge, Lensfield Road, Cambridge CB2 1EW, United Kingdom, [⊥]Department of Chemistry, Imperial College, Exhibition Road, London SW7 2AZ, United Kingdom, and [∥]Department of Materials Science and Engineering, The Ohio State University, Columbus, Ohio 43210, United States

ABSTRACT The aggregation of misfolded proteins is a common feature underlying a wide range of age-related degenerative disorders, including Alzheimer's and Parkinson's diseases. A key aspect of understanding the molecular origins of these conditions is to define the manner in which specific types of protein aggregates influence disease pathogenesis through their interactions with cells. We demonstrate how selenium-enhanced electron microscopy (SE-EM), combined with tomographic reconstruction methods, can be used to image, here at a resolution of 5−10 nm, the interaction with human macrophage cells of amyloid aggregates formed from Aβ_{25-36}, a fragment of the Aβ peptide whose self-assembly is associated with Alzheimer's disease. We find that prefibrillar aggregates and mature fibrils are distributed into distinct subcellular compartments and undergo varying degrees of morphological change over time, observations that shed new light on the origins of their differential toxicity and the mechanisms of their clearance. In addition, the results show that SE-EM provides a powerful and potentially widely applicable means to define the nature and location of protein assemblies *in situ* and to provide detailed and specific information about their partitioning and processing.

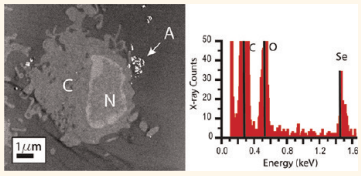

KEYWORDS: amyloid β · neurodegeneration · cytotoxicity · electron microscopy · macrophages

The deposition of proteins that have failed both to fold correctly and to be cleared successfully in organs and tissues is a pathological feature of many of the most common age-related degenerative diseases.[1,2] The formation of aggregates, often as well-defined amyloid structures, has been shown to play a central role in the pathogenesis of many of these conditions, of which Alzheimer's disease is the most common.[1,3] Consequently, much research has focused on defining the properties of protein aggregates and how these relate to their pathogenic effects *in vivo*. There are now, for example, several atomic level models of the structures of amyloid fibrils that have been obtained using various combinations of solution and solid-state NMR spectroscopy, X-ray diffraction, and cryo-electron microscopy (EM) techniques.[4−7] Such structural information has been vital in providing an understanding of the physicochemical properties underlying their formation and stability. However, much less information is available about the more heterogeneous precursors to these highly organized fibrils, despite the fact that these precursor species are now thought to be crucial elements in the pathogenesis of many amyloid diseases,[8−16] or about the nature of their interactions *in vivo* with cell organelles.

In order to address these vital aspects of our understanding of the relationship between protein aggregation and disease, we have set out to probe the detailed molecular structures of protein aggregates *in situ*, that is, within cells. Progress toward this goal has previously been made largely by using immunostaining with antibodies that detect specific conformational features of protein aggregates in combination with either fluorescence or transmission electron microscopy or by detecting changes in the properties of fluorescently tagged proteins as they aggregate.[17−24] Our aim is to build upon such studies and provide the type of nanoscale morphological information about aggregates *in vivo* that is provided by cryo-EM techniques *in vitro*.[25,26] Indeed, such techniques can provide information

* Address correspondence to a.porter@imperial.ac.uk, cmd44@cam.ac.uk, lml25@cam.ac.uk.

Received for review December 12, 2011 and accepted May 27, 2012.

Published online May 28, 2012
10.1021/nn204859e

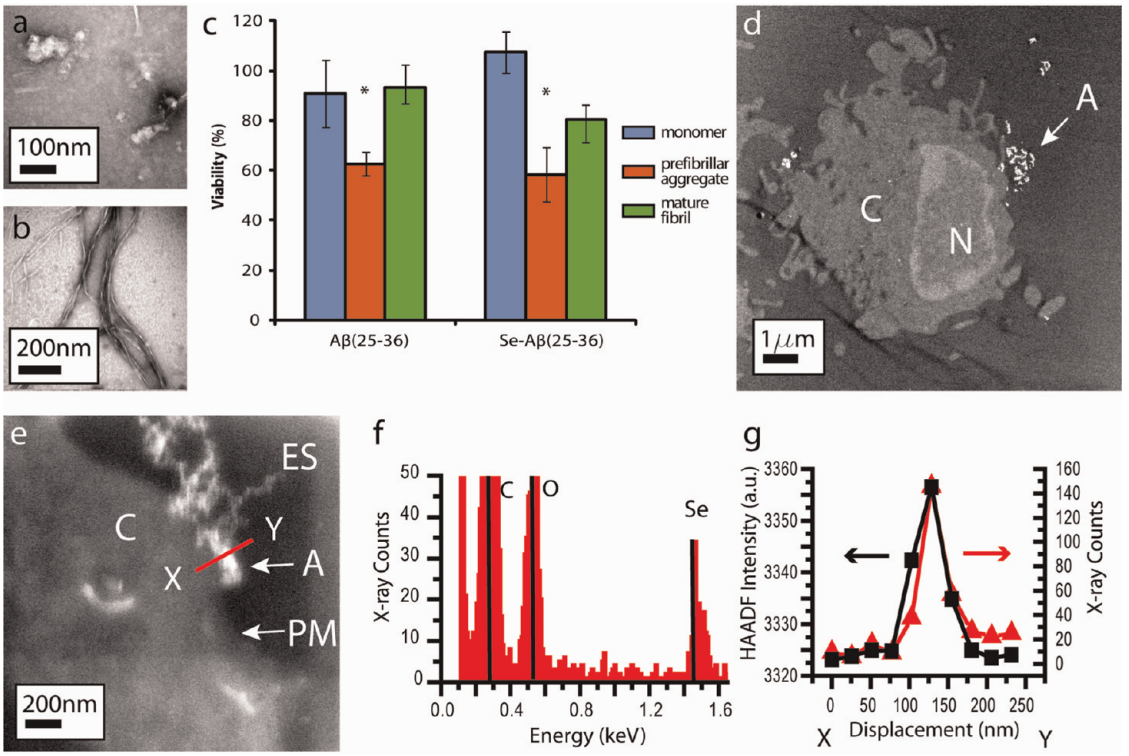

Figure 1. Characterization of Aβ_{25-36} aggregation and toxicity. Bright-field TEM images of Se-Aβ_{25-36} produced *in vitro* in (a) prefibrillar and (b) fibrillar forms. (c) Viability of HMMs exposed to Aβ_{25-36} with and without a selenium substitution at different stages of aggregation, as assessed by the MTT viability assay; * = statistically significant cytotoxicity ($p < 0.01$) when compared with cells exposed to buffer only. (d) HAADF-STEM image of HMMs exposed to mature fibrils of Se-Aβ_{25-36} for 24 h. (e) HAADF-STEM image showing fibrils in the vicinity of the cell membrane of an HMM. An EDX line spectrum was recorded through extracellular space, a fibrillar aggregate, and the cell cytoplasm, as indicated by the line XY. (f) EDX spectrum at the point of highest selenium EDX signal and highest HAADF signal along the line XY in (e). (g) Selenium profile and HAADF intensity profile along the line XY in (e). The X-ray counts within an energy window around the selenium peak in (f) were extracted along the same line; the peak in the presence of selenium corresponds to the peak in HAADF intensity. C = cytoplasm; N = nucleus; A = aggregates; ES = extracellular space; PM = plasma membrane. The data shown in (e–g) have been included in the proceedings of a conference.[39]

at the resolution of individual protein molecules, although they are challenging to apply in cellular systems because of the difficulties in visualizing carbon-rich protein aggregates within a carbon-rich environment.

To attempt to overcome this latter problem, we use a label-free EM technique,[27] which we term selenium-enhanced electron microscopy (SE-EM), to define as a function of time the subcellular location and the morphological features of individual aggregates of Aβ_{25-36} within human monocyte derived macrophage cells (HMMs). The underlying principle of SE-EM is that by substituting the naturally occurring sulfur atom in cysteine or methionine residues in a protein with selenium, an element of higher atomic number, the extent to which electrons interacting with the protein molecule undergo Rutherford scattering is significantly enhanced (by a factor of approximately 4.5 in this case).[27] Crucially, the selenium-substituted residues have extremely similar biochemical properties, resulting in few, if any, perturbations to the system. Indeed, the use of such substitutions to provide multiwavelength anomalous diffraction is a well-established tool in X-ray crystallographic protein structure determination.[28] In the context of electron microscopy, however, one can use high-angle annular dark-field scanning transmission electron microscopy (HAADF-STEM) to detect a selenium-substituted protein aggregate against its carbon-rich cellular environment without any extrinsic labeling or staining.[27]

Here we demonstrate how the SE-EM technique can be used to define subcellular localization and the morphological features of individual aggregates of Aβ_{25-36} within HMMs and to identify changes in their characteristics as a function of incubation time.

RESULTS AND DISCUSSION

We first generated *in vitro* aggregates of Aβ_{25-36} with a selenium atom incorporated into the methionine residue at position 35 in the sequence (Se-Aβ_{25-36}), a substitution which we have shown does not alter the rate of aggregation of the peptide as measured by thioflavin T fluorescence (Supporting Information Figure S1a). After 3 h of aggregation of Se-Aβ_{25-36} under the conditions used in this study, the major species present were observed by bright-field TEM to be heterogeneous prefibrillar aggregates (Figure 1a).

These prefibrillar species are clearly distinct in morphology from the mature fibrils (Figure 1b) that are the major species present at later times in the aggregation reaction, after *ca.* 12 h. Atomic force microscopy measurements reveal that the prefibrillar aggregates have heights ranging from 7 to 24 nm (mean 17.3 ± 4.2 nm, Supporting Information Figure S1d), whereas the fibrils have heights ranging from 4.5 to 9.5 nm (mean 6.3 ± 1.4 nm) and lengths of up to several hundred nanometers (Supporting Information Figure S1e).

The effects of addition of the different aggregated forms of both the Se-substituted and Se-free Aβ_{25-36} to HMMs were then explored (Figure 1c). For both Se-substituted and Se-free Aβ_{25-36}, neither the monomeric nor the fibrillar forms have significant effects on the viability of HMMs whether measured by the MTT [3-(4,5-dimethylthiazol-2-yl)-2,5-diphenyl tetrazolium bromide] or live/dead cell viability assays (Supporting Information Figure S2). By contrast, treatment with 10 μM of the prefibrillar forms of either Se-Aβ_{25-36} or its Se-free analogue causes significant reductions in the viability of HMMs (Figure 1c and Supporting Information Figure S2). These observations are consistent with previous reports on similar types of aggregates of a variety of systems indicating that prefibrillar oligomeric species have significantly greater toxicity than either the monomeric or fibrillar forms of proteins.[2,8−16]

To explore whether or not the different types of aggregates of Se-Aβ_{25-36} could be detected when added to HMMs, we next performed HAADF-STEM imaging of cells treated with fibrillar aggregates of Se-Aβ_{25-36} for 24 h. This approach revealed regions of high scattering intensity that are easily identifiable within the cellular environment (Figure 1d). The presence of selenium, as opposed to other atoms with high atomic numbers, such as iron, in regions of high scattering intensity was also confirmed using energy-dispersive X-ray (EDX) spectroscopy along a transect through the cell cytoplasm, a region of high scattering intensity, and the extracellular space (Figure 1e). The peak at 1.4 keV in the EDX spectrum collected at the point of highest HAADF image intensity confirms the presence of selenium (Figure 1f), and thus of the Se-Aβ_{25-36} peptide, at this location.

As the specific interactions of the electron beam with the specimens that dominate image contrast can be varied by altering image acquisition parameters, we collected images at high and low angles to observe how the mass and thickness of an object and the atomic composition of its constituent molecules affect the images. We note that at higher collection angles the contrast arises predominantly from the variations in the atomic number of the elements present, whereas at lower collection angles, variations in mass and thickness dominate the contrast of the image (Supporting Information Figure S3). This procedure allowed us to select the most suitable collection angles for each form of STEM imaging analysis undertaken in this work.

Having determined that aggregates of Se-Aβ_{25-36} can be clearly distinguished from the other components of the cellular environment, we proceeded to collect further images of fibrillar Se-Aβ_{25-36} aggregates, taken at periods of 2 and 24 h following their addition to HMMs, to investigate the changes in these species over time. After incubation for 2 h, the fibrillar species were observed predominantly on the outer surface of the plasma membrane (Figure 2a) and only occasionally inside the cell cytoplasm (Figure 2b). After 24 h of incubation, however, the aggregates appear to have lost their fibrillar structure and instead resemble irregular and amorphous structures (Figure 2c−l). Indeed, images of these aggregates (Figure 2c,d) suggest that they are now poorly defined species that appear to be at least partly degraded when compared to those fibrillar species observed in the extracellular space 2 h after their addition to the cells (Figure 2a). Twenty-four hours after the addition of fibrils to the HMM cells, aggregates are also visible within the cells. These intracellular aggregates have the appearance of condensed globular species and are located both within vesicles (Figure 2e,f) and within the cytoplasm (Figure 2h). Higher resolution images of these vesicular and cytoplasmic aggregates confirm their globular appearance and allow us to determine that they have diameters between 10 and 30 nm (Figure 2g,h). Strikingly, such globule-like species closely resemble structures of similar size and shape that are observed both in the aggregation and disaggregation[29] processes of amyloid fibrils *in vitro*, which are often described as oligomers or prefibrillar species.[8]

Addition of prefibrillar aggregates of Se-Aβ_{25-36} to cultures of HMMs reveals a very different behavior from that observed following addition of the fibrillar aggregates. After incubation for 2 h, the prefibrillar aggregates are observed not only to be in close proximity to the plasma membrane but also to be distributed throughout the cytoplasm and within intracellular vesicles (Figure 2i,j). Indeed, after 24 h of incubation with HMMs, the prefibrillar aggregates are found predominantly within intracellular vesicles (Figure 2k) and in the cytoplasm (Figure 2l−n) and even occasionally in the cell nucleus (Figure 2o,p). It is striking, however, that in contrast to the fibrillar species described above the appearance of these prefibrillar aggregates does not change significantly, even after 24 h of incubation with HMMs; in particular, observation of individual prefibrillar aggregates within the cytoplasm after 24 h shows that the aggregates have retained their globular appearance and their diameters have not changed significantly and still range from approximately 10−50 nm (Figure 2i−p).

As the precise localization of the aggregates in relation to the cell membrane, and intracellular compartment, can

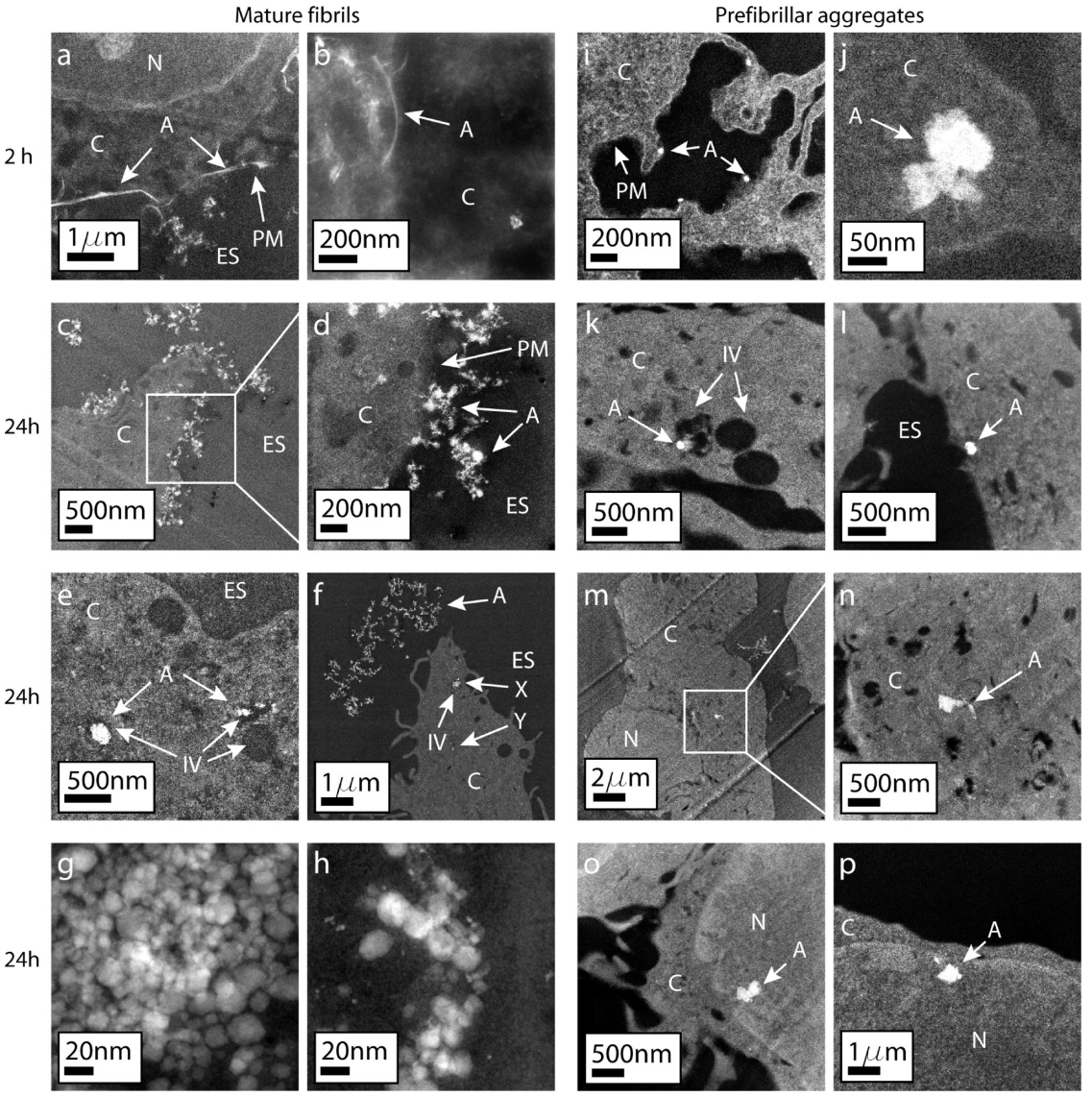

Figure 2. SE-EM imaging of Se-Aβ_{25-36} in HMMs. (a,b) HAADF-STEM images of HMMs exposed to mature Se-Aβ_{25-36} fibrils for 2 h showing (a) mature fibrils aligned with the plasma membrane and (b) a fibril within the cytoplasm of the cell. (c−f) HAADF-STEM images of HMMs exposed to mature fibrils of Se-Aβ_{25-36} for 24 h. The aggregates can be seen to be associated with the plasma membrane (c,d) and within intracellular vesicles (e,f); regions marked X (in an intracellular vesicle) and Y (in the cell cytoplasm) in (f) are shown at higher magnification in (g) and (h), respectively. (i,j) HAADF-STEM images of HMMs exposed to prefibrillar Se-Aβ_{25-36} aggregates for 2 h. (k−p) Examples of HAADF-STEM images of HMMs exposed to prefibrillar aggregates of Se-Aβ_{25-36} for 24 h. The aggregates are observed in intracellular vesicles (k), the cell cytoplasm (l−n), and the cell nucleus (o,p). C = cytoplasm; ES = extracellular space; A = aggregates; PM = plasma membrane; IV = intracellular vesicle; N = nucleus. (p) Included in proceedings of a conference.[40]

be difficult to determine unambiguously in two dimensions, we proceeded to analyze the location of both fibrillar and prefibrillar aggregates of Se-Aβ_{25-36} after 24 h of incubation with HMMs using 3D STEM tomography. The 3D tomographic reconstructions, both of sections and of whole freeze-dried cells treated with fibrillar aggregates, confirm that the fibrils are predominantly found in the vicinity of the plasma membrane after 24 h (Figure 3a−c). By contrast, prefibrillar species are observed to be distributed throughout the intracellular environment at this same time point rather than clustering at the cell surface (Figure 3d−f). Movies of all tomographic data sets are available in the Supporting Information.

These observations indicate that the distribution of aggregates differs significantly within HMMs that are exposed to prefibrillar or to mature fibrils and as a function of the time of exposure. To probe this phenomenon further, we undertook a quantitative analysis of the way in which localization of the two forms of aggregate varies with the time of exposure to the cells. This analysis revealed the following: (i) The majority of mature fibrils observed in each sample is located at the plasma membrane at every exposure time examined (Figure 4a), whereas the majority of the prefibrillar aggregates is always located within the cytoplasm (Figure 4b). (ii) The frequency with which mature fibrils

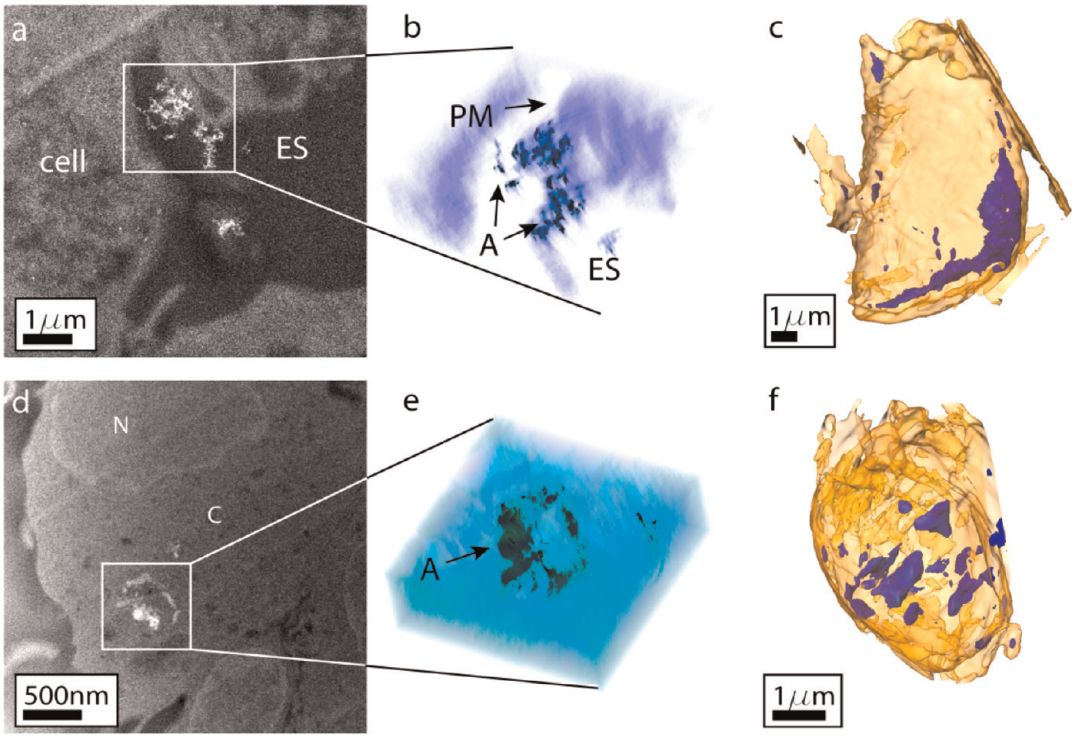

Figure 3. SE-EM tomographic reconstructions of Se-Aβ_{25-36} aggregates in cells. (a) HAADF-STEM image of an HMM that had been exposed to mature Se-Aβ_{25-36} fibrils for a period of 24 h. (b) Three-dimensional tomogram of the boxed area. Blue = cell, black = aggregates, white = extracellular space. (c) Three-dimensional reconstruction of a freeze-dried whole cell exposed to mature fibrils of Se-Aβ_{25-36}, yellow = cell, blue = aggregates. (d) HAADF-STEM image of a prefibrillar aggregate of Se-Aβ_{25-36} in the cytoplasm of an HMM. (e) Three-dimensional tomogram of the boxed area; blue = cytoplasm, black = aggregates. (f) Three-dimensional reconstruction of a freeze-dried cell; yellow = cell, blue = aggregates. ES = extracellular space; PM = plasma membrane; A = aggregate; N = nucleus; C = cytoplasm. (d,e) Included in the proceedings of a conference.[39]

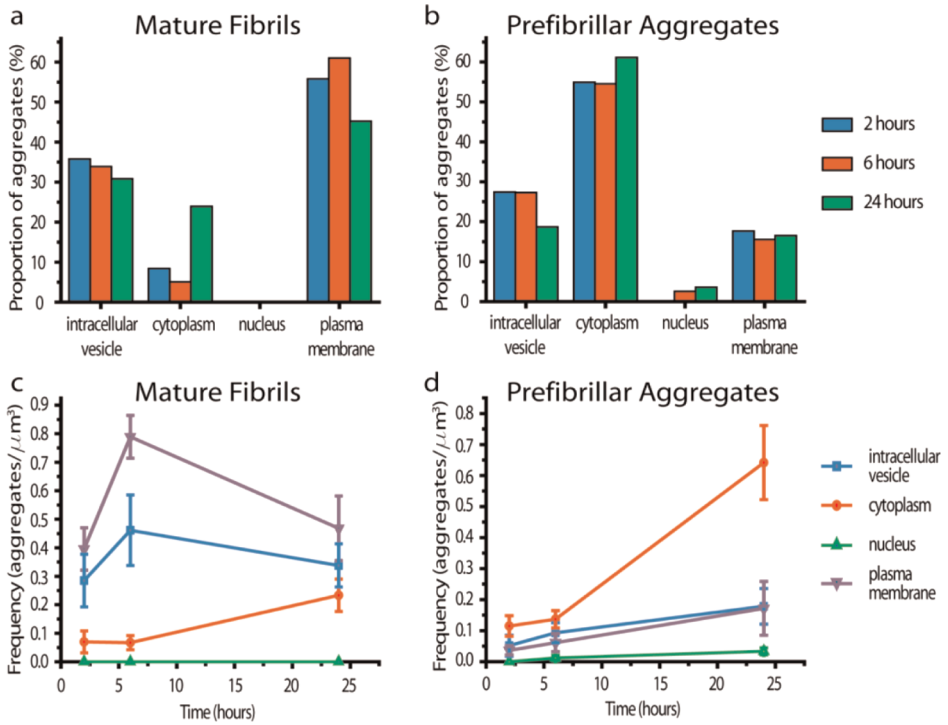

Figure 4. Time-dependent evolution of the subcellular distribution of Se-Aβ_{25-36} aggregates in cells. The data refer to HMMs following exposure to prefibrillar or fibrillar species for 2, 6, and 24 h. (a,b) Proportions of the total number of aggregates observed within each of the four indicated compartments of the cell after exposure to mature fibrillar aggregates (a) or prefibrillar aggregates (b). (c,d) Frequency with which the aggregates are observed in different subcellular locations as a function of the cell volume determined for mature fibrils (c) and prefibrillar aggregates (d). Error bars = SEM.

are observed at the plasma membrane and in intracellular vesicles reaches its maximum value after 6 h of exposure before declining (Figure 4c); the latter observation is likely to reflect clearance of these aggregates from the cells. By contrast, the frequency with which prefibrillar aggregates are observed in all of the locations examined continues to increase with time, reflecting their progressive accumulation within the cells (Figure 4d). (iii) Although fibrillar aggregates or their degradation products are never observed in the nucleus, prefibrillar aggregates are occasionally observed in this organelle. Together, these observations demonstrate that exposure of HMMs to prefibrillar and fibrillar aggregates results in very different preferences for their sites of interaction with the cell, and that the dynamics of their distributions throughout the cells are also quite different.

CONCLUSION

The use of the SE-EM technique in this study has allowed us to begin to probe the relationships between the structure and location of specific aggregates of an amyloidogenic peptide, here Aβ_{25-36}, and their toxic effects. Of particular significance is the finding that when prefibrillar species and mature amyloid fibrils are taken up into cells, they are distributed into distinct subcellular compartments where they undergo varying degrees of morphological change over time; such differences are very likely to be strongly related to differences in their intrinsic toxicity[8−16] and the mechanisms of their clearance.[30] Additional studies in which SE-EM is applied to other systems, including the full length Aβ peptides, and to other cell types and even whole tissues should, therefore, have the potential to provide detailed insights into these systems, particularly in conjunction with complementary studies involving techniques such as optical imaging.[17,20,24] Additionally, the SE-EM strategy can be extended further by using recombinant protein strategies that enable the production of seleno-containing proteins; these strategies include the use of cysteine/methionine auxotrophic cell lines as well as novel biosynthetic incorporation strategies, which offer the possibility of site-specific labeling of individual amino acids. Similarly, a range of protein transduction techniques are available that would enable the ready import of seleno-containing proteins into live cells.[31,32] The combination of the techniques described here with new cryo-machining methods capable of generating thin intracellular lamellae will also open the door to the study of protein assemblies inside eukaryotic cells at molecular scale resolution.[33] Therefore, the present results reinforce the view[27] that SE-EM has the potential to become a generally applicable method to study protein assemblies *in situ* as well as to enhance significantly our view of how protein aggregates interact with cells and, consequently, our understanding of the origin and progression of the neurodegenerative conditions whose prevalence is increasing dramatically in the modern world.

MATERIALS AND METHODS

Peptide Preparation and Aggregation. All Aβ_{25-36} peptides generated through solid-phase synthesis were purchased from Bachem (Weil am Rhein, Germany). Se-substituted peptides were synthesized by the same method used for the natural peptide, but with methionine being replaced with selenomethionine during the synthesis process. Solutions of the Aβ_{25-36} peptides were prepared by dissolving the freeze-dried peptides in TFA/HFIP, a method that efficiently disrupts any preformed aggregates present in the solutions.[34] The peptides were then dissolved in 50 mM sodium phosphate buffer at pH 7.4, with 100 mM NaCl, to give a protein monomer concentration of 100 μM. Aliquots of these solutions were added to the cell medium immediately after dissolution in buffer or following incubation at 37 °C for specified periods of time.

Exposure of Cells and Viability Assays. Isolation and culture of HMMs were carried out as described previously.[35,36] The MTT assay, in which the reduction of 3-(4,5-dimethylthiazol-2-yl)-2,5-diphenyl tetrazolium bromide] (MTT) by cells is measured to give a measure of their mitochondrial function and thus the number of healthy cells, was carried out following a previously published protocol[35] as was the live/dead viability assay, in which the incorporation of propidium iodide into the nuclei of dead cells is compared to the incorporation of Hoechst, which binds to the nuclei of all cells, in order to assess the percentage of cells that are viable.[35] Statistical analysis was performed using a two-tailed type 2 *t* test with significance set at $p < 0.01$.

Cells for electron microscopy analysis were seeded in 6-well tissue culture plates at between 4×10^6 and 8×10^6 cells/well. Solutions containing Se-Aβ_{25-36} aggregates at a protein concentration of 10 μM (based on the concentration of protein monomers) were added to the cell culture medium, and after periods of 2, 6, or 24 h of exposure to the Aβ_{25-36} peptide solutions, cell fixation and embedding was carried out following a previously published protocol.[35,36]

Electron Microscopy. Sections of fixed and embedded cells were cut with an ultramicrotome using a 35° wedge angle diamond knife and floated on distilled water. Sections were immediately collected on uncoated 300 mesh copper grids (Agar Scientific, Stansted, UK) and dried for 30 min at 37 °C. Sections of 70−100 nm thickness were used for imaging studies, and thicker (200−300 nm) sections were used for STEM tomography analysis. In order to visualize entire cells in the electron microscope using 3D STEM tomography, freeze-dried HMMs were prepared following a previously published technique.[36] Bright-field TEM imaging was performed on a JEOL 2000 microscope operating at 120 kV. HAADF-STEM imaging was carried out on an FEI Titan 80/300 aberration-corrected TEM/STEM microscope operating at 300 kV with a STEM probe size of approximately 0.24 nm. Inner and outer HAADF collection angles of 8 to 33 mrad and 41 to 161 mrad, respectively, were used. All statistical analyses and imaging were performed on three different cell exposures, and hundreds of cell profiles were surveyed from each exposure. In the EDX analysis in Figure 1, a selenium peak was collected at 1.4 keV from 10 different regions of the Se-Aβ_{25-36} peptide. This analysis was performed on three different exposures.

STEM Tomography. Electron tomography of thick sections (200−300 nm) of resin-embedded cells was carried out in STEM mode using inner and outer collection angles of approximately 13 and 64 mrad, respectively. Images were collected at tilt angles ranging from −50 to +50° using a step size of 2°, at

a resolution between 2.5 and 4.0 nm/pixel, a pixel dwell time of 20 μs, and an electron dose rate between 4 and 5 $\times$ 10^6 A/m^2. In order to prevent the presence of intracellular organelles complicating the detection of protein aggregates, tomography of freeze-dried whole cells was carried out using inner and outer collection angles of approximately 32 and 160 mrad, respectively. Images were collected at tilt angles ranging from -70 to $+70°$ using a step size of 2° up to $\pm 50°$ and 1° at higher tilt angles; images were collected at a resolution of 10$-$15 nm/pixel, a pixel dwell time of 30 μs, and an electron dose rate between 4 and 5 $\times$ 10^6 A/m^2. Three-dimensional reconstruction was carried out using a simultaneous iterative reconstruction technique (SIRT)[37,38] using Inspect3D (FEI, Eindhoven, The Netherlands). Three-dimensional volumes were visualized using Amira visualization software (Amira, Berlin, Germany).

Visualization of the 3D reconstructions of freeze-dried whole cells was carried out by creating isosurfaces based on the intensity levels of regions within each tomographic data set. A transparent isosurface was created at one intensity level to represent the whole cell, and another opaque isosurface was created at a higher intensity level to represent only those regions within the cell volume that were of particularly high intensity. This procedure means that the cell membrane appears to be outside the selenium-enhanced aggregates in cells that have been exposed to fibrils because the scattering intensity of the aggregates falls away gradually rather than disappearing instantly, partly as a result of the averaging that occurs in the reconstruction process and partly due to the method of data collection; the images used to create the tomographic data sets were collected at relatively low magnification where it is not possible to distinguish the various morphologies of the aggregates. This effect is also compounded by the averaging that occurs in the data reconstruction procedure; thus the areas of high intensity appear as large amorphous regions rather than as distinct aggregates.

Quantification of the Subcellular Distribution of Aggregates. Quantification of the intracellular distribution of Se-Aβ_{25-36} aggregates was carried out by mapping out randomly located areas of cell sections and collecting overlapping STEM images. Maps were reconstructed, and the total cross sectional area of the cells examined was measured by thresholding using ImageJ (NIH, Maryland, USA). The cross sectional area was then multiplied by the section thickness to give the volume of cell examined. The mapped out areas were subdivided into 10 smaller areas containing approximately equal cell volumes, and the number aggregates in each of the four subcellular locations—in an intracellular vesicle, in the cell cytoplasm, in the cell nucleus, or associated with the cell membrane—were counted. The frequency with which aggregates were observed in each subcellular location for each of the 10 selected fields was then calculated by dividing the number of aggregates observed by the cell volume. Statistical analysis was carried out on these values to give a mean, standard deviation and standard error. In order to exclude the possibility of including iron or ferritin granules in the assessment of the number of aggregates present only those aggregates that had at least one dimension of at least 50 nm were counted. An aggregate was classified as being in an intracellular vesicle if resin (having an intensity similar to that of the extracellular space) was visible between the aggregates and the cell cytoplasm. The number of aggregates in each location was also calculated as a percentage of the total number of aggregates counted to give the relative abundance of aggregates in the different subcellular compartments.

Atomic Force Microscopy (AFM). Samples were drop-cast onto mica substrates and allowed to dry. Tapping mode AFM was carried on all samples using a nanoscope IV microscope (Nanoscope IV) using Pointprobe silicon cantilevers (purchased from Windsor Scientific, Slough, U.K.).

Conflict of Interest: The authors declare no competing financial interest.

Acknowledgment. Some data relating to parts of this study have been previously presented at scientific conferences including Figure 1e$-$g,[39] Figure 2p,[40] Figure 3d,e,[39] and Supporting Information Figure S3a,b.[39] This research was supported by a Titan Grant EPSRC (EP/C51596X), a European starting grant for AP (Project number 257182), The Wellcome Trust, FEI Life Sciences Division, the BBSRC for L.L. and an ART grant for B.B. We would like to thank Lisa Cabrita for many extremely helpful discussions of this work.

Supporting Information Available: Detailed experimental procedures and supplementary images and movies. This material is available free of charge *via* the Internet at http://pubs.acs.org.

REFERENCES AND NOTES

1. Chiti, F.; Dobson, C. M. Protein Misfolding, Functional Amyloid, and Human Disease. *Annu. Rev. Biochem.* **2006**, *75*, 333–366.
2. Stefani, M.; Dobson, C. M. Protein Aggregation and Aggregate Toxicity: New Insights into Protein Folding, Misfolding Diseases and Biological Evolution. *J. Mol. Med.* **2003**, *81*, 678–699.
3. Kelly, J. W. Towards an Understanding of Amyloidogenesis. *Nat. Struct. Mol. Biol.* **2002**, *9*, 323–325.
4. Fandrich, M.; Meinhardt, J.; Grigorieff, N. Structural Polymorphism of Alzheimer Aβ and Other Amyloid Fibrils. *Prion* **2009**, *3*, 89–93.
5. Jimenez, J. L.; Nettleton, E. J.; Bouchard, M.; Robinson, C. V.; Dobson, C. M.; Saibil, H. R. The Protofilament Structure of Insulin Amyloid Fibrils. *Proc. Natl. Acad. Sci. U.S.A.* **2002**, *99*, 9196–9201.
6. Sunde, M.; Serpell, L. C.; Bartlam, M.; Fraser, P. E.; Pepys, M. B.; Blake, C. C. F. Common Core Structure of Amyloid Fibrils by Synchrotron X-ray Diffraction. *J. Mol. Biol.* **1997**, *273*, 729–739.
7. Tycko, R. Molecular Structure of Amyloid Fibrils: Insights from Solid-State NMR. *Q. Rev. Biophys.* **2006**, *39*, 1–55.
8. Bucciantini, M.; Calloni, G.; Chiti, F.; Formigli, L.; Nosi, D.; Dobson, C. M.; Stefani, M. Prefibrillar Amyloid Protein Aggregates Share Common Features of Cytotoxicity. *J. Biol. Chem.* **2004**, *279*, 31374–31382.
9. Cleary, J. P.; Walsh, D. M.; Hofmeister, J. J.; Shankar, G. M.; Kuskowski, M. A.; Selkoe, D. J.; Ashe, K. H. Natural Oligomers of the Amyloid-β Protein Specifically Disrupt Cognitive Function. *Nat. Neurosci.* **2005**, *8*, 79–84.
10. Ferreira, S. T.; Vieira, M. N. N.; De Felice, F. G. Soluble Protein Oligomers as Emerging Toxins in Alzheimer's and Other Amyloid Diseases. *IUBMB Life* **2007**, *59*, 332–345.
11. Haass, C.; Selkoe, D. J. Soluble Protein Oligomers in Neurodegeneration: Lessons from the Alzheimer's Amyloid-β Peptide. *Nat. Rev. Mol. Cell Biol.* **2007**, *8*, 101–112.
12. Karpinar, D. P.; Balija, M. B. G.; Kügler, S.; Opazo, F.; Rezaei-Ghaleh, N.; Wender, N.; Kim, H.-Y.; Taschenberger, G.; Falkenburger, G. H.; Heise, H.; *et al.* Pre-fibrillar α-Synuclein Variants with Impaired β-Structure Increase Neurotoxicity in Parkinson's Disease Models. *EMBO J.* **2009**, *28*, 3256–3268.
13. Baglioni, S.; Casamenti, F.; Bucciantini, M.; Luheshi, L. M.; Taddei, N.; Chiti, F.; Dobson, C. M.; Stefani, M. Prefibrillar Amyloid Aggregates Could Be Generic Toxins in Higher Organisms. *J. Neurosci.* **2006**, *26*, 8160–8167.
14. Bucciantini, M.; Giannoni, E.; Chiti, F.; Baroni, F.; Formigli, L.; Zurdo, J. S.; Taddei, N.; Ramponi, G.; Dobson, C. M.; Stefani, M. Inherent Toxicity of Aggregates Implies a Common Mechanism for Protein Misfolding Diseases. *Nature* **2002**, *416*, 507–511.
15. Li, S. M.; Hong, S. Y.; Shepardson, N. E.; Walsh, D. M.; Shankar, G. M.; Selkoe, D. Soluble Oligomers of Amyloid-β Protein Facilitate Hippocampal Long-Term Depression by Disrupting Neuronal Glutamate Uptake. *Neuron* **2009**, *62*, 788–801.
16. Selkoe, D. J. Soluble Oligomers of the Amyloid-β Protein Impair Synaptic Plasticity and Behavior. *Behav. Brain Res.* **2008**, *192*, 106–113.
17. Badman, M. K.; Pryce, R. A.; Charge, S. B.; Morris, J. F.; Clark, A. Fibrillar Islet Amyloid Polypeptide (Amylin) Is Internalised by Macrophages but Resists Proteolytic Degradation. *Cell Tissue Res.* **1998**, *291*, 285–294.

18. Ard, M. D.; Cole, G. M.; Wei, J.; Mehrle, A. P.; Fratkin, J. D. Scavenging of Alzheimer's Amyloid-β Protein by Microglia in Culture. *J. Neurosci. Res.* **1996**, *43*, 190–202.
19. Argiles, A.; Garcia, M.; Mourad, G. Phagocytosis of Dialysis-Related Amyloid Deposits by Macrophages. *Nephrol., Dial., Transplant.* **2002**, *17*, 1136–1138.
20. Chafekar, S. M.; Baas, F.; Scheper, W. Oligomer-Specific Aβ Toxicity in Cell Models is Mediated by Selective Uptake. *Biochim. Biophys. Acta* **2008**, *1782*, 523–531.
21. Kaminski-Schierle, G. S.; van de Linde, S.; Erdelyi, M.; Esbjörner, E. K.; Klein, T.; Rees, E.; Bertoncini, C. W.; Dobson, C. M.; Sauer, M.; Kaminski, C. F. *In Situ* Measurements of the Formation and Morphology of Intracellular β-Amyloid Fibrils by Super-Resolution Fluorescence Imaging. *J. Am. Chem. Soc.* **2011**, *133*, 12902–12905.
22. Koenigsknecht, J.; Landreth, G. Microglial Phagocytosis of Fibrillar β-Amyloid through a β1 Integrin-Dependent Mechanism. *J. Neurosci.* **2004**, *24*, 9838–9846.
23. Paresce, D. M.; Chung, H. Y.; Maxfield, F. R. Slow Degradation of Aggregates of the Alzheimer's Disease Amyloid-β Protein by Microglial Cells. *J. Biol. Chem.* **1997**, *272*, 29390–29397.
24. Weltzien, R. B.; Pachter, J. S. Visualization of β-Amyloid Peptide (Aβ) Phagocytosis by Human Mononuclear Phagocytes: Dependency on Aβ Aggregate Size. *J. Neurosci. Res.* **2000**, *59*, 522–527.
25. Sachse, C.; Fandrich, M.; Grigorieff, N. Paired β-Sheet Structure of an Aβ(1−40) Amyloid Fibril Revealed by Electron Microscopy. *Proc. Natl. Acad. Sci. U.S.A.* **2008**, *105*, 7462–7466.
26. Schmidt, M.; Sachse, C.; Richter, W.; Xu, C.; Fandrich, M.; Grigorieff, N. Comparison of Alzheimer Aβ(1−40) and Aβ(1−42) Amyloid Fibrils Reveals Similar Protofilament Structures. *Proc. Natl. Acad. Sci. U.S.A.* **2009**, *106*, 19813–19818.
27. Porter, A. E.; Knowles, T. P. J.; Muller, K. H.; Meehan, S.; McGuire, E. K.; Skepper, J. N.; Welland, M. E.; Dobson, C. M. Imaging Amyloid Fibrils within Cells Using a Se-Labelling Strategy. *J. Mol. Biol.* **2009**, *392*, 868–871.
28. Hendrickson, W. A.; Pähler, A.; Smith, J. L.; Satow, Y.; Merritt, E. A.; Phizackerley, R. P. Crystal Structure of Core Streptavidin Determined from Multiwavelength Anomalous Diffraction of Synchrotron Radiation. *Proc. Natl. Acad. Sci. U.S.A.* **1989**, *86*, 2190–2194.
29. Narayan, P.; Orte, A.; Clarke, R. W.; Bolognesi, B.; Hook, S.; Ganzinger, K. A.; Meehan, S.; Wilson, M. R.; Dobson, C. M.; Klenerman, D. The Extracellular Chaperone Clusterin Sequesters Oligomeric Forms of the Amyloid-β_{1-40} Peptide. *Nat. Struct. Mol. Biol.* **2012**, *19*, 79–83.
30. Mandrekar, S.; Jiang, Q.; Lee, C. Y. D.; Koenigsknecht-Talboo, J.; Holtzman, D. M.; Landreth, G. E. Microglia Mediate the Clearance of Soluble Aβ through Fluid Phase Macropinocytosis. *J. Neurosci.* **2009**, *29*, 4252–4262.
31. Van den Berg, A.; Dowdy, S. F. Protein Transduction Domain Delivery of Therapeutic Macromolecules. *Curr. Opin. Biotechnol.* **2011**, *22*, 888–893.
32. Kaminski Schierle, G. S.; Bertoncini, C. W.; Chan, F. T. S.; van der Goot, A. T.; Schwendler, S.; Skepper, J.; Schlachter, S.; van Ham, T.; Esposito, A.; Kumita, J. R.; *et al.* A FRET Sensor for Non-Invasive Imaging of Amyloid Formation *in Vivo*. *ChemPhysChem* **2011**, *12*, 673–680.
33. Rigort, A.; Bäuerlein, F. J. B.; Villa, E.; Eibauer, M.; Laugks, T.; Baumeister, W.; Plitzko, J. M. Focused Ion Beam Micromachining of Eukaryotic Cells for Cryoelectron Tomography. *Proc. Natl. Acad. Sci. U.S.A.* **2012**, *109*, 4449–4454.
34. Teplow, D. B.; Indu, K.; Ronald, W. *Preparation of Amyloid-β Protein for Structural and Functional Studies*; Academic Press: Waltham, MA, 2006; pp 20−33.
35. Motskin, M.; Wright, D. M.; Muller, K.; Gard, T. G.; Skepper, J. N. Hydroxyapatite Nano and Microparticles: Correlation of Particle Properties with Cytotoxicity and Biostability. *Biomaterials* **2009**, *30*, 3307–3317.
36. Porter, A. E.; Muller, K. H.; Skepper, J. N.; Midgley, P.; Welland, M. Uptake of C60 by Human Monocyte Macrophages, Its Localization and Implications for Toxicity: Studied by High Resolution Electron Microscopy and Electron Tomography. *Acta Biomater.* **2006**, *2*, 409–419.
37. Kak, A. C.; Slaney, M. *Principles of Computerized Tomographic Imaging*; IEEE Press: New York, 1988.
38. Gilbert, P. Iterative Methods for the Three-Dimensional Reconstruction of an Object from Projections. *J. Theor. Biol.* **1972**, *36*, 105–117.
39. McGuire, E. K.; Motskin, M.; Knowles, T. P. J.; Dobson, C. M.; McComb, D. W.; Porter, A. E. Imaging Alzheimer's Disease-Related Protein Aggregates in Human Cells Using a Selenium Label. *J. Phys. Conf. Ser.* **2010**, *241*, 012020.
40. McGuire, E. K.; Motskin, M.; Dobson, C. M.; Porter, A. E.; McComb, D. W. Substitutionally Enhanced STEM (SE-STEM) Imaging of Protein Aggregates Inside Cells. *Microsc. Microanal.* **2011**, *17*, 174–175.